



Mesoporous anatase crystal-silica nanocomposites with large intrawall mesopores presenting quite excellent photocatalytic performances



Weiyang Dong^{a,*}, Li Li^a, Xin Chen^a, Youwei Yao^a, Yankun Ru^a, Yaojun Sun^b, Weiming Hua^c, Guoshun Zhuang^a, Dongyuan Zhao^c, Shuwen Yan^a, Weihua Song^a

^a Department of Environmental Science and Engineering, Fudan University, 2005 Songhu Road, Shanghai 200438, PR China

^b Center for Analysis and Measurement, Fudan University, 2005 Songhu Road, Shanghai 200438, PR China

^c Department of Chemistry, Fudan University, 2005 Songhu Road, Shanghai 200438, PR China

ARTICLE INFO

Keywords:
Preparation
Mesoporous nanocomposites
Anatase crystal-silica
Tunable intrawall mesopores
Photocatalysis

ABSTRACT

Mesoporous anatase crystal-silica nanocomposites with three-dimensional (3D) uniform and tunable intrawall mesopores connecting the mesochannels have been successfully prepared using the approach of first synthesizing titania-silica nanocomposites with ordered two-dimensional hexagonal mesochannels via “synchronous-assembly” of inorganic precursors with surfactant, then “extracting silica”. The uniform intrawall pores can be finely tuned in 3.6–5.6 nm by the strategy of adopting a large amount of silica in the walls, a very high crystallization temperature and mild silica extraction. The 3D interconnectivities of the mesochannels increase with extraction, but the mesostructures are retained intact. The average size of uniform anatase nanocrystals is 11.2 nm. This method is moderate, simple and facilely reproducible. The diffusion efficiencies of methylene blue (MB) in the mesostructures elevate with the intrawall mesopore size. The transient steady-state concentrations of •OH radicals rise fast with the intrawall pore size. The degradation rate of MB on the representative photocatalyst possessing large intrawall mesopores is extremely high (0.372 min^{-1}), which is as high as 7.3 times that on the parent material, even up to 38.8 times that upon P25 photocatalyst. Our results clearly illustrate that the large intrawall mesopores play an overwhelming role in the increments of activities, while the matched adsorbability play an important synergetic role. Additionally, our photocatalysts are quite stable and reusable. Such results have not been seen in the literature till now. Furthermore, this approach is generally applicable to other metal-oxides-based materials, opening up a new avenue to rationally design and prepare mesostructures with 3D large intrawall mesopores, suitable adsorption and unexpected photocatalytic performances.

1. Introduction

Almost 80% of the world's population confront high levels of threat to water security, millions of people die per year (27,300 children a week) from diseases transmitted through unsafe water, and water contamination problems are expected to grow worse in the coming decades globally [1–3]. Dyes are one sort of the major contaminants in water bodies. Every year, about one million tons of various dyes (more than 100,000) are manufactured worldwide [4–6], and approximately 280,000 tons of textile dyes are released into the environment through effluent discharges such as dyeing, printing and finishing, etc. [7,8]. The dyes in water bodies have been regarded as one of the most important environmental pollutants, and are of great concern for both toxicological and esthetic reasons [7–11]. Cationic dyes (also called basic dyes) are a very important category of all commercial dyes, which

are water soluble and widely used in the dyeing of textile, paper and leather, etc. Basic dyes are reported to be the brightest class of soluble dyes with very high tinctorial values, and the dyes with lower than 1 ppm in water can generate an obvious coloration [12,13]. Most of them are potential or known human carcinogens even at low concentrations [12,13]. Methylene blue (MB) is an important cationic dye because it is widely used in the textile industry and represents a class of dyestuffs resistant to biodegradation [6,13,14].

Conventional approaches like coagulation, flocculation, etc. have been employed to handle cationic dye-containing wastewaters. But, many drawbacks still exist in these techniques, such as producing large amounts of sludge, difficulties in the full color removal and expensiveness [7,12]. Conventional biological treatments can't often effectively decolorize and degrade the cationic dyes, due to a great degree of aromatics in the molecules and their inherent reluctance to

* Corresponding author.

E-mail address: wydong@fudan.edu.cn (W. Dong).

biodegradation [7]. It is capable to remove basic dyes for the membrane separation, however, the principal limitations are the high cost, the lowered productivity with time due to fouling of the membrane and the treatment of concentrates [7,12,15]. Adsorption of activated carbon is an effective method, but it is an expensive means mainly for the non-renewable use, etc. [16–18].

Many new and more powerful technologies have been developed for removing the cationic dyes in the past decades globally, including photocatalysis [7–9,14,15,19], photoelectrocatalysis [20], combination of photocatalysis and biofilm [21], processes of Fenton, photo-Fenton and electro-Fenton [6,7,22], chemical oxidations (such as oxidations of ozonation, hypochlorite ion, etc.) [7], oxidations of electrochemistry and photoelectrochemistry [7], etc. Among these technologies, heterogeneous photocatalysis has emerged as one of the most powerful methods of water decontamination due to its potential to transform recalcitrant organic contaminants into mineral salts and relatively innocuous end products such as carbon dioxide and water, etc. [8,23]. So far, TiO₂-based photocatalytic technique has been recognized as the most effective, environmentally friendly and promising method, and countless researches have been focused on it [24–35]. Of which the ordered mesoporous titania-based materials have drawn great interests because of their mesochannels and high specific surface areas [26–35], etc.

It is well-known that the mesoporous structures with 3D interconnections possess many remarkable advantages over that without interlinking [36–41]. In the 3D interconnected mesopore architectures, large intrawall mesopores (larger than the size of primary mesochannels) connecting the mesochannels have the following striking superiorities over the small counterparts (\leq the mesochannels' size) linking the channels. First, the large intrawall mesopores are more beneficial for guest molecules to enter and depart the mesochannels networks. Secondly, the diffusion efficiency of guest molecules in the mesostructural networks will be higher. Thirdly, light harvesting efficiency will be higher due to the multiple scattering of light in the large-intrawall-pore-connecting mesochannels [42–44], etc. These prominent merits can more highly effectively enhance the photocatalytic performances. In addition, the controls of phase, crystal size and crystallinity of the framework are also important issues, because they decide the performances in practical applications [36,37]. For instance, TiO₂ has three crystalline phases, of which the anatase polymorph shows the top photocatalytic activity [26]. Both high crystallinity and large nanocrystals can distinctly raise activity [26,34]. Moreover, the matched adsorbability with mesopore architectures and photocatalytic performances can further markedly improve activity [34,35,39,45], etc. The synergistic influence of all the above features can hugely enhance the photocatalytic performances. However, so far the reports about the ordered mesoporous metal-oxides-based materials with 3D large intrawall mesopores connecting the mesochannels, large nanocrystals and fit adsorbability are very few in the literature, because it is hard to be prepared.

In this study, we first synthesized anatase crystal-silica nanocomposites with ordered two-dimensional (2D) hexagonal mesochannels array using “synchronous-assembly” of surfactant and inorganic precursors molecules, then created uniform and tunable intrawall pores linking the mesochannels in 3D means via “extracting silica”. Our strategy is the employing of a large amount of SiO₂ in the walls, a very high crystallization temperature and moderate extraction, aiming at obtaining large and uniform intrawall mesopores and anatase nanocrystals. Based on this strategy, the uniform intrawall pore size can be finely tuned in a range of 3.6–5.6 nm and enlarges gradually with extraction time. The mesochannels are connected into 3D networks by the intrawall mesopores, and the interconnectivity elevates with extraction, but the mesostructures are maintained in their integrities and regularities. TiO₂ is complete anatase crystalline with uniform and big nanocrystals (11.2 nm in size). This method is gentle, uncomplicated and can be easily repeated. MB was chosen as a model contaminant.

The photocatalytic results indicate that our mesostructured composites with 3D large intrawall mesopores display considerable excellent photocatalytic degradation activities to MB, which are greatly higher than that of the parent sample and Degussa commercial P25 photocatalyst, in addition to being quite stable and reusable. To the best of our knowledge, these results have not been reported in the literature up to now. The fundamentals of this study would provide new insights for the design and preparation of other mesoporous metal-oxides-based composites with large intrawall pores and photocatalytic performances beyond expectations, etc.

2. Experimental section

2.1. Chemicals

Titanium isopropoxide [Ti(OCH(CH₃)₂)₄, TIPO, $\geq 97\%$] and tetraethyl orthosilicate [Si(OC₂H₅)₄, TEOS, $\geq 96\%$] were purchased from Fluka. Pluronic P123 [$M_w = 5800$, EO₂₀PO₇₀EO₂₀] was received from Aldrich. Ethanol (absolute), concentrated HCl (36.5 wt.%), NaOH (96%) were AR grade and purchased from Shanghai Chemical Corp. P25 photocatalyst (A commercial nano-crystalline TiO₂ consisting of ca. 80% anatase and 20% rutile; BET area $\text{ca. } 50 \text{ m}^2 \text{ g}^{-1}$) was kindly supplied by Degussa Corp. Methylene blue (MB, C₁₆H₁₈ClN₃S·3H₂O, 97%, the molecular structure is shown in Fig. S1, Supplementary material) bought from Sinopharm was prepared into $5.0 \times 10^{-5} \text{ M}$ solution with deionized water. All the chemicals were used as received without any further purification.

2.2. Synthesis

The ordered 2D hexagonal mesoporous titania-silica nanocomposite (such as Ti/Si molar ratio = 60/40, 100/0) was synthesized using TIPO as TiO₂ precursor, TEOS as SiO₂ precursor and P123 as a template according to the “synchronous-assembly” process of surfactant and inorganic precursors molecules [33]. The samples as-synthesized were calcined at 350 °C for 6 h in air to remove the organic template, subsequently crystallized at 1000 °C and 450 °C (for pure TiO₂) for 2 h in air with a heating rate of 1 °C min⁻¹, respectively. Thus, the ordered 2D hexagonal mesoporous anatase TiO₂-SiO₂ nanocomposite and TiO₂ were obtained and finely ground, which was then treated with diluted NaOH solution (such as 0.5 M) at 40 °C according to a solid/liquid ratio of 1/10 (g mL⁻¹) to “extract silica” [39]. The mixture in a sealed beaker was vigorously stirred for 12 h, then the suspension was centrifuged to recover the solid. A certain amount of specimen was separated from the solid as the product, while the residual was again impregnated in the newly taken NaOH solution using the same solid/liquid ratio as the above. This procedure was repeatedly progressed under the identical conditions. It needed to be indicated that a certain amount of sample was taken out from the recovered solid in each cycle. The products were thoroughly washed with deionized water under stirring, centrifuged, followed by dried at 100 °C for 24 h, then activated at 300 °C for 3–6 h in air with a heating rate of 3 °C min⁻¹, respectively.

2.3. Characterization

2.3.1. X-ray powder diffraction

Small-angle X-ray powder diffraction (SAXRD) patterns were recorded on a German Bruker D4 X-ray diffractometer with Ni-filtered Cu-K α radiation (40 kV, 40 mA). Wide-angle X-ray diffraction (WAXRD) were collected on a Rigaku D/MAX-rB X-ray powder diffractometer using a high-power Cu-K α ($\lambda = 0.15418 \text{ nm}$) source operating at 40 kV and 60 mA with a graphite monochromator filter. The average size of anatase nanocrystals was estimated by using the Scherrer's equation to the half-height width of the 101 diffraction peak with silicon as a standard for the instrumental line broadening. The crystallinity of anatase nanocrystals was expressed with the intensity of the 101

diffraction peak.

2.3.2. Transmission electron microscopy (TEM)

TEM images were obtained on a JEM-2011 transmission electron microscope (JEOL Company) combined with energy dispersive X-ray spectroscopy (EDX) operating at 200 kV. For TEM measurements, the samples were prepared by sonication in ethanol and suspended on holey carbon grids. The contents of Ti and Si atoms in the samples were examined using energy dispersive X-ray spectroscopy (EDX).

2.3.3. N_2 adsorption-desorption isotherms

N_2 adsorption-desorption isotherms were collected on a Micromeritics ASAP 2010 Adsorption Analyzer at -196°C (77 K). The samples were degassed at 250°C for at least 5 h before analyses. The Brunauer–Emmett–Teller (BET) specific surface areas were calculated from adsorption data at a relative pressure range from 0.057 to 0.20. The total pore volumes (V_T) were calculated at a relative pressure of 0.976. Pore size distributions were calculated from adsorption branches using Barrett–Joyner–Halenda (BJH) method.

2.3.4. Fourier-transform infrared (FT-IR)

Investigations of surface hydroxyl groups and acidic properties of the samples were performed on a Nicolet Fourier-transform infrared (FT-IR) NEXUS 470 spectrometer using a quartz IR cell equipped with CaF_2 windows. The samples finely ground were pressed into uniform self-supporting wafers and then placed into the holder. The samples were degassed at 300°C under a vacuum ($< 1 \times 10^{-3}$ Torr) for 4 h to remove water and other impurities, and then cooled down to room temperature (ca. 20°C). Before adsorbing pyridine, the spectra were recorded to evaluate the number of surface hydroxyl groups. The samples were then exposed to a saturated vapor of pyridine at room temperature (20°C) for 20 min, thereafter, degassed at 150°C under the vacuum for 30 min. The spectra were recorded to evaluate the number of acid sites.

2.3.5. Ultraviolet-visible diffuse reflectance spectra (UV-vis DRS)

UV-vis DRS were obtained with a JASCO V-550 UV-vis spectrophotometer equipped with integrating sphere attachment using BaSO_4 as a reference. The band gaps (E_g) were estimated by extrapolating to zero a linear fit to the plots of the square root of Kubelka–Munk functions against $h\nu$ of the light [34,46,47].

2.3.6. Adsorption and photocatalytic oxidation

Adsorption and photocatalytic oxidation of MB on the mesoporous titania–silica nanocomposites with 3D intrawall mesopores were investigated in air in a quartz vessel at room temperature according to our previous method [35,39,40]. 50 mL of MB aqueous solutions and 50.00 mg of the catalyst powders finely ground were placed in the quartz vessel, which formed a suspension under stirring. For comparison, all the experiments were carried out under the identical conditions. The suspensions were vigorously stirred first in dark for a certain time to evaluate the adsorption performances. After establishing adsorption–desorption equilibrium, UV light irradiation was turned on. The photocatalytic reactions were carried out under UV light irradiation from a 25 W low-pressure mercury lamp ($\lambda = 254\text{ nm}$). The radiant flux was measured with a photometer (International Light Model IL1400A). 1.0 mL of suspensions were taken at given time intervals and centrifuged at 15,000 rpm for 15 min. The concentrations of MB were analyzed using a JASCO V-550 UV-vis spectrophotometer. For comparison, the performances of ordered 2D mesoporous titania–silica nanocomposites and P25 photocatalyst were also measured.

2.3.7. TOC measurement

50 mL of MB aqueous solutions and 50.00 mg of the catalyst powders finely ground were placed in the quartz vessel, which formed a suspension under stirring. The suspensions were vigorously stirred first

in dark for a certain time. After establishing adsorption–desorption equilibrium, UV light irradiation was turned on. For comparison, the suspensions tested for TOC were prepared under the identical conditions as that of the adsorption and photocatalytic oxidation, and as each other. The suspensions were taken out at given time intervals and centrifuged at 15,000 rpm for 15 min. The TOC content of the bulk solutions was monitored with a Shimadzu TOC-L CPH CH200 TOC analyzer. Potassium hydrogen phthalate and a mixture of sodium hydrogen carbonate and sodium carbonate were used to quantify the total carbon (TC) and inorganic carbon (IC), respectively. The TOC was calculated subtracting IC from TC. The percentage of TOC removal (%) = $(\text{TOC}_0 - \text{TOC}_t) \times 100 / \text{TOC}_0$, where TOC_0 is the TOC of the initial solution and TOC_t is the TOC of the solution at time t .

2.3.8. Stability and reusability

Stability and reusability were investigated by repetitively adsorbing and degrading MB. After the MB molecules were adsorbed and photocatalytically degraded each time, the catalyst was separated by centrifugation, followed by activating at 300°C in air for 3–6 h. Subsequently, it was reused in the same concentration of MB solution.

2.3.9. Transient steady-state concentrations of $\cdot\text{OH}$ radicals

Transient steady-state concentrations of $\cdot\text{OH}$ radicals generated by the samples in the aqueous solutions were measured using *p*-chlorobenzoic acid (pCBA) as a $\cdot\text{OH}$ -probe compound. pCBA solution (3.00 mg L^{-1}) and 1.00 mg mL^{-1} of the finely ground sample powders were placed in the quartz vessel to form a suspension under vigorous stirring, respectively. The suspensions were vigorously stirred first in dark for a certain time to evaluate the adsorption performance. After establishing adsorption–desorption equilibrium, UV light irradiation was turned on. About 1.25 mL of suspensions were taken out at timed intervals and centrifuged at 15,000 rpm for 10 min. The supernatants (about 0.8 mL) were analyzed using high-performance liquid chromatography (HPLC) for the quantification of pCBA. Separation and analysis were performed with an Agilent Series 1260 system equipped with a diode array detector (DAD) operated at 236 nm. An injection volume to a C18 column ($5 \mu\text{m}$, $4.6 \times 250 \text{ mm}$, Phenomenex, Gemini C18) at 30°C was $100 \mu\text{L}$, and the HPLC was carried out under reverse phase condition. The mobile phase in isocratic method with a flow rate of 1 mL min^{-1} , a mixture of 70% Methanol + 30% DI (with 0.05% TFA) in water, was used to analyze the samples. $\ln(C_0/C)$ was plotted versus the photocatalytic reaction time (t); where, C is the pCBA concentration at time t and C_0 is the pCBA concentration at adsorption–desorption equilibration before light on. A straight line can be achieved and the slope is the apparent first-order rate constant (k_{obs}) [$\ln(C_0/C) = k_{\text{obs}} \times t$]. Thus, the transient steady-state concentration of $\cdot\text{OH}$ radicals can be calculated from the formula $k_{\text{obs}} = k_{\cdot\text{OH}/\text{pCBA}} \times [\cdot\text{OH}]_{\text{ss}}$; where, $k_{\cdot\text{OH}/\text{pCBA}} = 5 \times 10^9 \text{ M}^{-1}\text{s}^{-1}$ (the second-order rate constant for reaction of pCBA with $\cdot\text{OH}$) [39].

3. Results and discussion

3.1. SAXRD and WAXRD

There is only one diffraction peak (2 theta: 1.09°) on the SAXRD pattern of the parent sample (SA1) [Fig. 1Aa], which can be indexed as the 100 reflection of typical 2D hexagonal mesoporous architecture (space group $p6mm$) [33], being an indication of an ordered arrangement of mesochannels with a cell parameter (a_0) of 9.3 nm . When silica was extracted for 24 h, the intensity, position (1.09°) and width of the diffraction peak essentially have no changes [Fig. 1Ab], demonstrating that the mesostructural regularity remains intact. With further progress of the extraction, although the diffraction peaks widen gradually, there are still no big variations for the intensities and positions [Fig. 1A(c–f)], illustrating that the ordered mesostructures are kept yet.

The characteristic diffraction peaks of anatase phase, especially the

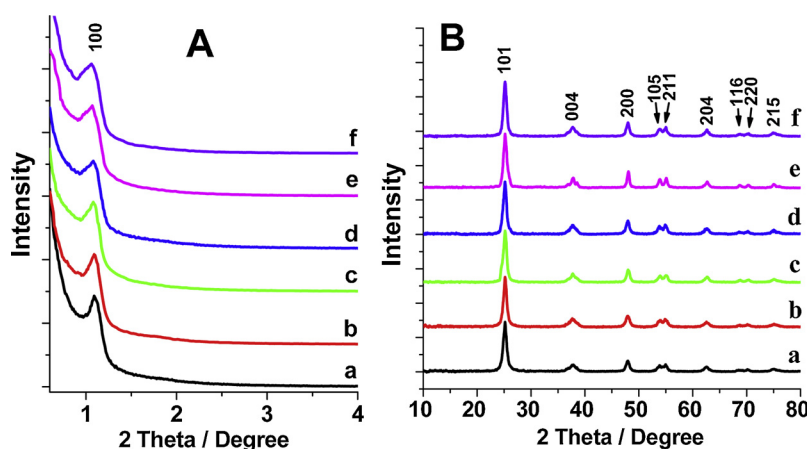


Fig. 1. SAXRD (A) and WAXRD (B) patterns of the samples after extracting silica from the 2D hexagonal mesoporous titania-silica nanocomposite for 0 h (the parent sample, SA1) (a), 24 h (SA2) (b), 36 h (SA3) (c), 48 h (SA4) (d), 60 h (SA5) (e) and 72 h (SA6) (f), respectively.

Table 1

Physicochemical properties of the samples after extracting silica for various times from the anatase crystal-silica nanocomposite with ordered 2D hexagonal mesoporous structure.

Samp. name	Extraction time ^a , h	TiO ₂ /SiO ₂ molar ratio	Intensity of 101 peak ^b	Area of 101 peak ^c	Average pore size ^d , nm	Mean pore size ^e , nm	S ^f , m ² g ⁻¹	V _T ^g , mL g ⁻¹	Average crystal size ^h , nm
SA1	0	59.7/40.3	287	281	4.1	4.1	83	0.121	11.3
SA2	24	70.3/29.7	290	276	3.6, 4.1	3.4, 4.1	108	0.142	11.2
SA3	36	74.9/25.1	298	276	4.2, 4.2	3.9, 4.2	118	0.149	11.3
SA4	48	79.4/20.6	307	279	4.8, 4.2	4.5, 4.2	126	0.156	11.2
SA5	60	85.8/14.2	310	277	5.3, 4.2	5.0, 4.2	144	0.170	11.1
SA6	72	90.0/10.0	316	277	5.6, 4.2	5.3, 4.2	157	0.181	11.2

^a Extraction time with diluted NaOH solution at 40 °C.

^b Intensity of 101 diffraction peak on WAXRD pattern is stood for with its height.

^c Area of the 101 diffraction peak on WAXRD pattern.

^d The data came from the HRTEM observations. The left and right data are the sizes of the intrawall mesopores and mesochannels, respectively.

^e The data were obtained from the adsorption branches of N₂ isotherms. The left and right data are the sizes of the intrawall mesopores and mesochannels, respectively.

^f BET specific surface areas.

^g Total pore volumes.

^h The data were obtained by measuring the crystals size from the HRTEM images, then calculating the average value.

narrow and intense 101 peak appear on the WAXRD pattern of the sample SA1 without other peaks [Fig. 1Ba] [33], indicating that the crystalline phase is anatase. The intensity and area of 101 diffraction peak are 287 and 281 (Table 1), respectively. The average size of anatase crystals is calculated to be 10.8 nm, larger than the cell parameter (9.3 nm). It means that such sized crystals may protrude into the cylindrical mesochannels, and hence obstruct some channels in part or whole. After silica being extracted for 24 h, there are no big variations in both the intensity and area of the 101 diffraction peak [Fig. 1Bb, Table 1], which are demonstrations of essentially no alterations in the crystallinity and nanocrystals size. As the silica extraction continues to progress, the intensity of 101 diffraction peak strengthens gradually, but the peak areas essentially remains unchanged [Fig. 1B(c–f), Table 1], which clearly illustrate that the crystallinities of the samples increase little by little, while the crystals size basically maintains unaltered under our mild extraction conditions.

3.2. TEM observations

Viewed along [001] and [110] directions, TEM images show that the parent sample (SA1) has straight cylindrical mesopore channels in ordered 2D hexagonal arrangement without pores in the walls [Fig. 2]. The cell parameter (a_0) is evaluated to be 9.4 nm, nearly the same as that (9.3 nm) calculated from the SAXRD pattern. The mesochannels are very uniform in size and the average size is measured to be 4.1 nm.

High-resolution TEM (HRTEM) images further reveal that the crystals orientations are random and the crystals link with the amorphous silica nanoparticles mutually to form a very unique framework structure [Fig. 2(c–d)]. Most of the crystals overlap each other on the pore walls, while some thrust into the mesochannels to engender “ink-bottle-shape-like” or blocked channels [Fig. 2(c–d), marked with red square frames]. The sizes of crystals are uniform and the average size is measured to be 11.3 nm, slightly bigger than 10.8 nm calculated from the WAXRD patterns. The crystals lattice fringes can be clearly observed and an average d -spacing is measured to be 0.34 nm, which is indexed as the 101 reflection of anatase structure, according with the d_{101} spacing (0.35 nm) calculated from the WAXRD patterns. It is worth mentioning that the amorphous silica nanoparticles are large in size and dense [Fig. 2(c–d)].

Interestingly, images of SA2 show that large number of pores appear in the walls after extracting SiO₂ for 24 h [Fig. 3, some were marked]. Some “peanuts-shell-shaped” pore channel openings can be distinctly viewed along [001] direction. The intrawall pores of high density can similarly be clearly observed along [110] direction. Although the intrawall pores are randomly oriented, they always connect the mesochannels to create 3D hexagonal bimodal interpenetrated mesochannel networks. The distribution of intrawall pore sizes is rather narrow (3.1–4.2 nm) and the average size is 3.6 nm. Some silica particles have been taken the place of by the intrawall mesopores. HRTEM observations disclose that many occluded mesochannels are opened by

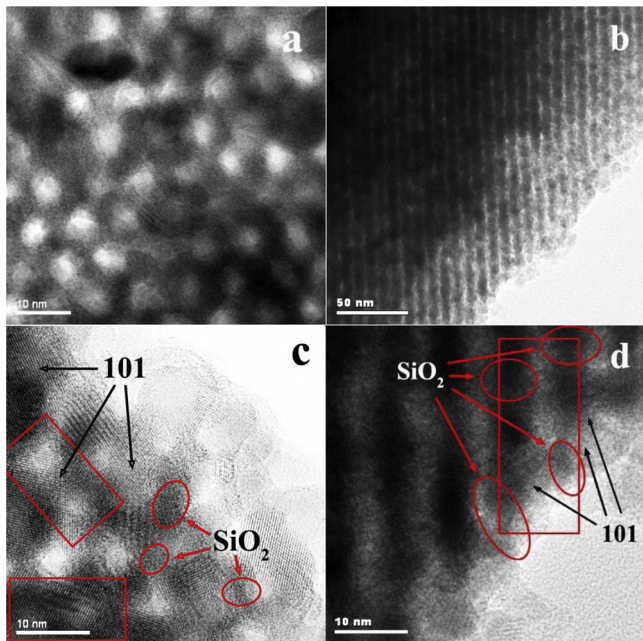


Fig. 2. Representative TEM (b) and HRTEM (a, c–d) images of the mesoporous anatase crystal-silica nanocomposite with ordered 2D hexagonal array (the parent sample, SA1); viewed along [001] (a, c) and [110] (b, d) directions, respectively.

the intrawall mesopores, and looking like “ink-bottle-shaped” pores (some were marked). The average size of mesochannels is measured to be 4.1 nm, the same as that of SA1. The average size of uniform anatase nanocrystals is measured to be 11.2 nm, almost the same as that (11.3 nm) of SA1. With continuing of silica extraction, TEM images

show that the average sizes of intrawall mesopores and the interconnectivities of mesochannels increase gradually, but the pore size distributions are still quite narrow [Table 1, Figs. S2–S5]. More and more blocked mesochannels are opened even by three or more intrawall mesopores [some were marked with red square frames]. Nevertheless, the mesopore architectures are still retained their integrities and regularities, which are further confirmed by the SAXRD results. Noteworthy, the sizes of the intrawall mesopores (4.8–5.6 nm) are bigger than that of the mesochannels (4.2 nm) when the extraction times are equal to or longer than 48 h. EDX analysis of the parent material shows that the Ti/Si molar ratio is 59.7/40.3 [Table 1, Fig. S6a], being well in accordance with that (60/40) added in the synthesis sol. After silica extraction for 24 h, the Ti/Si ratio rises to 70.3/29.7 [Table 1, Fig. S6b]. With the progress of extraction, the Ti/Si ratio continues to elevate obviously [Table 1, Fig. S6(c–f)], but the mesopore architectures have no collapses [Figs. 1A(c–f), S2–S5]. Our results further show that there are no intrawall pores in the mesoporous pure TiO_2 after extracting for 48 h [Fig. S7], which evidently illustrates that the extraction can't create pores in the walls of the mesoporous TiO_2 under our experimental conditions.

3.3. N_2 adsorption-desorption isotherms

N_2 adsorption isotherm of the parent composite presents typical type IV curve with one capillary condensation step in a relative pressure (p/p_0) range of 0.40–0.56 [Fig. 4Aa], which is a suggestion of a narrow distribution of mesochannel sizes. The hysteresis loop displays H2 type, which implies an ink-bottle-shaped mesochannels geometry. This may be in relations with any mesochannels blockage from the piercing of anatase nanocrystals [33], consistent with the TEM observations [Fig. 2(a–d)]. The mean channels size is about 4.1 nm [Fig. 4Ba, Table 1], the same as that (4.1 nm) evaluated from HRTEM observations (Table 1). BET specific surface area and pore volume calculated

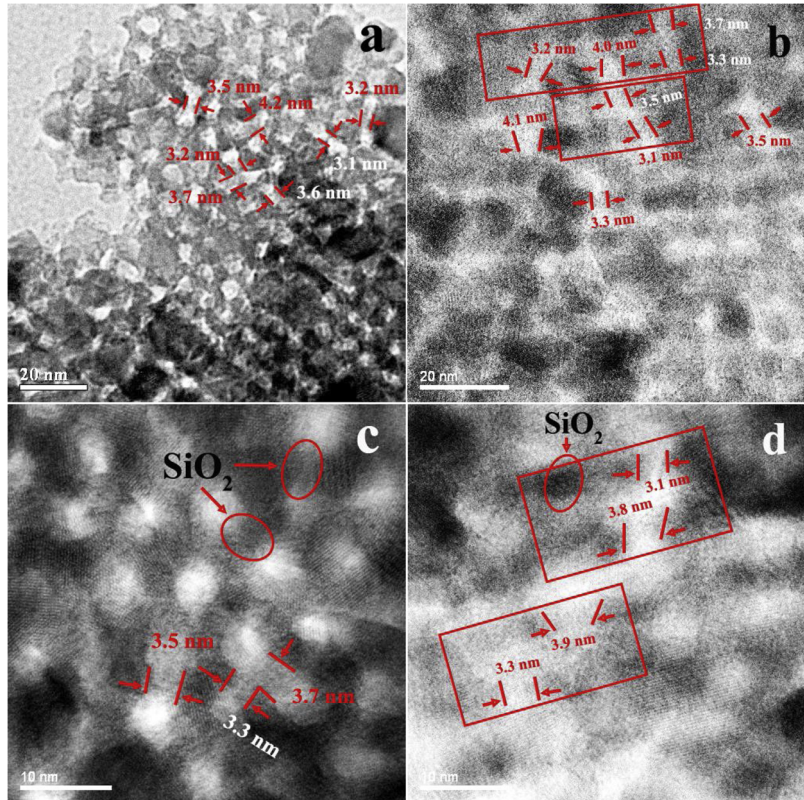
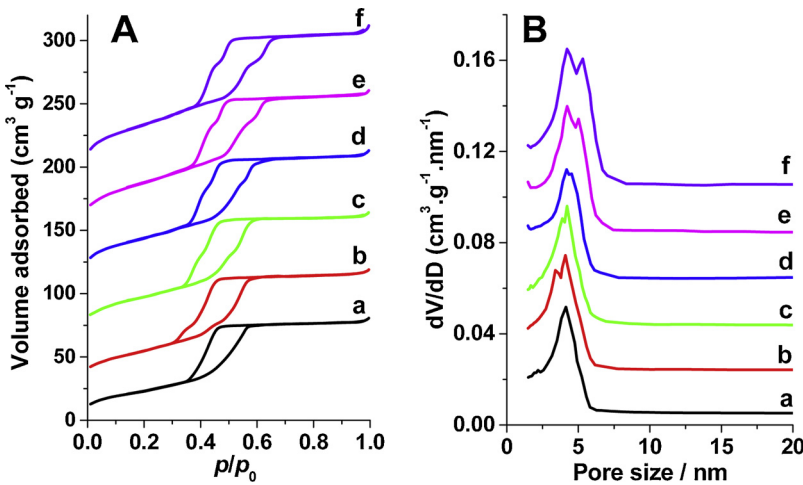


Fig. 3. Representative TEM (a) and HRTEM (b–d) images of the sample SA2 after extracting silica for 24 h from the parent SA1; viewed along [001] (a, c) and [110] (b, d) directions, respectively.



are 83 m² g⁻¹ and 0.121 cm³ g⁻¹, respectively.

Very interestingly, the sample SA2 exhibits two obvious capillary condensation steps on the N₂ adsorption curve [Fig. 4Ab], which are evident suggestions of two sets of mesopores with varying size. The new and weak N₂ uptake in low p/p_0 region (0.40–0.46) indicates the existence of small mesopores with a very narrow pore size distribution. The N₂ uptake in the 0.48–0.58 p/p_0 region is markedly steeper than that of SA1, implying an augment of the mesopore channels, which probably result from the opened mesochannels. It is worth noting that the isotherms display an incorporated hysteresis loop (consisting of two interpenetrated hysteresis loops), which also present H2 type. The desorbed amount in 0.30–0.36 p/p_0 region is relatively small, which should be caused by the intrawall pores. The drop of desorbed amount in 0.37–0.46 p/p_0 region is sharper than that of the parent specimen, which is a suggestion of an increment of the ink-bottle-shaped mesochannels and should be attributed to the opened mesochannels. The curve of pore size distribution presents two discrete and well-resolved peaks [Fig. 4Bb]. The weak peak located at ca. 3.4 nm is rather narrow, which is a clear indication of very uniform intrawall mesopores in size. The mean size of mesochannels (ca. 4.1 nm) is the same as that of SA1. The above results are well coincident with the TEM observations. The specific surface area (108 m² g⁻¹) and pore volume (0.142 cm³ g⁻¹) are remarkably larger than that of SA1 [Table 1, Fig. S8], respectively. With silica extraction, both the two N₂ uptakes rise gradually [Fig. 4A(c–f)], which suggest increments of the intrawall mesopores and mesochannels in number. The positions of N₂ uptakes stemmed from the intrawall

Fig. 4. N₂ adsorption-desorption isotherms (A) and pore size distributions (B) of the samples after extracting silica from the parent material for 0 h (SA1) (a), 24 h (SA2) (b), 36 h (SA3) (c), 48 h (SA4) (d), 60 h (SA5) (e) and 72 h (SA6) (f), respectively. The isotherms of (b–f) are offset vertically by 25, 65, 109, 148 and 190 cm³ g⁻¹, respectively.

mesopores shift to higher p/p_0 region gradually, until to 0.61–0.66 p/p_0 region, while the relative p/p_0 regions of N₂ uptakes caused by the mesochannels nearly have no changes (0.47–0.57). These demonstrate that the sizes of intrawall mesopores increase progressively, but the mesochannels sizes maintain unvaried roughly. The hysteresis loops transform from H2 type to H1 gradually, especially when the times of extraction are equal to or longer than 48 h [Fig. 4A(c–f)], suggesting a transformation from the ink-bottle-shaped mesochannels to non-ink-bottle-shaped ones [33], and should be owed to the large intrawall mesopores. The weak peaks strengthen remarkably, but the widths vary inconspicuously [Fig. 4B(c–f)], suggesting that the number of intrawall mesopores increases, but the pore size distributions are still quite narrow. The intrawall pore sizes enlarge gradually and are even larger than that of the mesochannels (4.2 nm) after the extraction times are equal to or longer than 48 h [Fig. 4B(c–f), Table 1]. There are no big alterations for the mesochannels in size and distribution. The BET specific surface areas and pore volumes are in the ranges of 118–157 m² g⁻¹ and 0.149–0.181 cm³ g⁻¹, respectively, enlarging remarkably with SiO₂ removal [Table 1, Fig. S8]. These results prove once again that the mesostructures have not collapse using our mild silica extraction. All these results are in good accordance with that from TEM and SAXRD measurements.

3.4. In-situ FT-IR spectra

FT-IR spectrum of the parent material (SA1) shows a quite strong

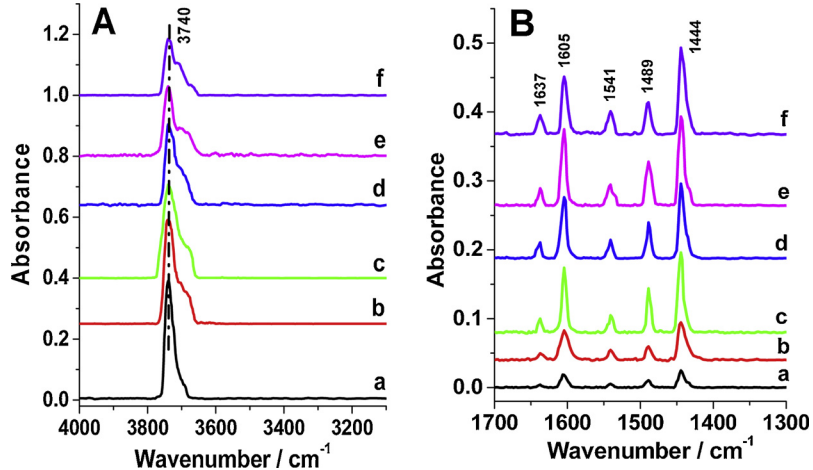


Fig. 5. In-situ FT-IR spectra for the surface hydroxyl groups (A) and acid sites (B) on the samples after extracting SiO₂ from the ordered 2D hexagonal mesoporous anatase crystal-silica nanocomposite for 0 h (SA1) (a), 24 h (SA2) (b), 36 h (SA3) (c), 48 h (SA4) (d), 60 h (SA5) (e) and 72 h (SA6) (f), respectively.

Table 2

The numbers of Si–OH groups and acid sites on the sample surfaces, and bandgap energies of the samples.

Sample name	Extraction time, h	TiO ₂ /SiO ₂ molar ratio	Sample weight, mg	S _{OH/g} ^a	De temp. of pyrid. ^b , °C	Band areas of pyridine adsorbed			E _g ^f , eV
						S _{LA/g} ^c 1444 cm ⁻¹	S _{BA/g} ^d 1541 cm ⁻¹	S _{TA/g} ^e	
SA1	0	59.7/40.3	9.2	1405	150	31	5	36	3.00
SA2	24	70.3/29.7	12.9	1287	150	60	11	71	2.99
SA3	36	74.9/25.1	15.0	1180	150	75	14	89	2.98
SA4	48	79.4/20.6	11.8	1054	150	94	18	112	3.00
SA5	60	85.8/14.2	12.7	904	150	107	25	132	3.00
SA6	72	90.0/10.0	11.7	788	150	121	30	151	3.00

^a Absorbance band area of surface hydroxyl groups per gram of sample calculated from the integrated areas of FT-IR spectra and sample weight.

^b Desorption temperature of pyridine.

^c Absorbance band area of pyridine adsorbed on Lewis acid sites per gram of sample.

^d Absorbance band area of pyridine adsorbed on Brönsted acid sites per gram of sample.

^e Absorbance band area of pyridine adsorbed on total acid sites per gram of sample (Lewis and Brönsted acids, S_{LA} + S_{BA}).

^f Bandgap energy.

absorbance band in the range of 3800–3600 cm⁻¹ (centered at ~3740 cm⁻¹) [Fig. 5Aa], which is assigned to the surface Si–OH groups stretching vibration [34], illustrating that large numbers of silica particles or silicon atoms are located on the surface. The band area of surface hydroxyl groups per gram of sample is calculated to be 1405 [Table 2, Figs. 5Aa, S9]. The area of absorbance band per gram of sample SA2 is 1287 [Table 2, Figs. 5Ab, S9], indicating that the number of surface Si–OH groups declines greatly compared with SA1. The band areas continue to decrease remarkably with silica extraction [Table 2, Figs. 5A(c–f), S9], illustrating that the number of surface silanol groups drops significantly, also suggesting dramatic declines of adsorption centers [34,39].

FT-IR spectrum of pyridine adsorption on the sample SA1 presents several characteristic bands [Fig. 5Ba], which are attributed to the pyridine adsorbed on Lewis acid sites (exposed Ti⁴⁺ cations, 1444 and 1605 cm⁻¹) and Brönsted acid sites (associated with Ti–O–Si bridges, 1541 and 1637 cm⁻¹) [34,39], respectively, demonstrating the existence of a number of acid sites on the surface. The band areas of pyridine adsorbed on Lewis and Brönsted acid sites per gram of sample are calculated to be 31 and 5 (Table 2), respectively. For the sample SA2, the band areas of pyridine adsorbed on Lewis (60) and Brönsted acid sites (11) enlarge obviously [Fig. 5Bb, Table 2, Fig. S10], respectively, which are about twice that on SA1, illustrating distinct augmentations of acid sites in number. With the removal of silica, the areas of pyridine adsorbed on both Lewis and Brönsted acid sites continue to increase evidently [Fig. 5B(c–f), Table 2, Fig. S10], implying the numbers of both Lewis and Brönsted acid sites increase remarkably, which are perhaps caused by both the increases of exposed Ti⁴⁺ atoms and Ti–O–Si linkages on the surfaces due to the declines of SiO₂ and the obvious enlargements of specific surface areas (Table 1).

3.5. UV-vis DRS

The spectrum of SA1 presents a considerable strong absorbance under 400 nm [Fig. 6Aa], the bandgap energy is measured to be 3.0 eV [Fig. 6Ba, Table 2]. Compared with SA1, the absorbance and bandgap energy (2.99 eV) of SA2 essentially have no changes [Fig. 6(A, B)b, Table 2]. With silica extraction, both the absorbances and bandgap energies similarly have no big alterations [Fig. 6(A, B) (c–f), Table 2]. These results clearly indicate that the absorbance and bandgap structures of anatase TiO₂ have not been changed during the whole process of silica removal.

3.6. Preparation strategy of large intrawall mesopores

The titania-silica nanocomposites with ordered 2D hexagonal mesopore structures were first synthesized using the “synchronous-

assembly” of inorganic precursors with surfactant molecules, combined with the processes of template removal at low temperature and pore walls crystallization at high temperature [Fig. S11]. The samples synthesized possess a uniform, homogeneous and amorphous framework with well-dispersed titanate and silicate [Fig. S11A]. Upon calcination at 350 °C to remove the surfactant molecules, the amorphous pore walls begin to crystallize. At that moment, phase separation takes place and anatase nanocrystals are randomly embedded in the matrices of amorphous titania and silica [Fig. S11B]. The nanocrystals coarsen with further temperature rising and/or time elongating. Meanwhile, the amorphous silica nanoparticles also enlarge, which serve as a glue fastening the anatase nanocrystals to form very unique “brick-mortar-like” pore walls [Fig. S11C]. In addition, the silica nanoparticles play a vital role in stabilizing the mesopore architectures, limiting quick growth of the nanocrystals and restraining the transformation of anatase-to-rutile phase even at 1000 °C. Therefore, the ordered 2D hexagonal mesoporous anatase crystal-silica nanocomposites [Fig. 7A] with full anatase crystallization, large and uniform nanocrystals and silica nanoparticles (which are the decisive factors to the size of intrawall mesopores) can be readily obtained by adjusting and controlling the Ti/Si ratio, temperature and time of crystallization, etc. In this work, our strategy is to use a large amount of SiO₂ and a very high crystallization temperature in order to obtain large and uniform anatase nanocrystals and silica nanoparticles in the walls. Then, the intrawall mesopores with large and tunable sizes highly linking the mesochannels in 3D networks can be obtained via “mild extracting silica” [Fig. 7B]. Based on this strategy, the large intrawall mesopores, particularly larger than the mesochannels’ size, can be not only obtained, but the integrity and regularity of the mesostructures, crystallinity and nanocrystals size can be retained intact as well. Accordingly, the performances of photocatalytic degradation on the materials can be greatly enhanced.

3.7. Adsorption and photocatalytic degradation of MB

The adsorption efficiency of MB on SA1 (the parent sample) without intrawall mesopores is relatively low, it takes approximately 22 min to essentially reach adsorption-desorption equilibrium [Fig. 8Aa]. The adsorption amount of saturation (AAS) is about 39.4% [Figs. 8Aa, S12, S13]. For the sample SA2 with intrawall mesopores of about 3.6 nm in size linking the mesochannels in 3D way, the adsorption efficiency is elevated obviously, it shortens to ca. 10 min to attain the equilibration [Fig. 8Ab], which should be owed to the contribution of mesopores in the walls. But the AAS (35.8%) is evidently lower than that of the parent sample [Figs. 8Ab, S12, S13]. With the enlargement of intrawall mesopores sizes (4.2–5.6 nm), the diffusion efficiencies of MB are further enhanced and the equilibrium time reduces to 1.5 min

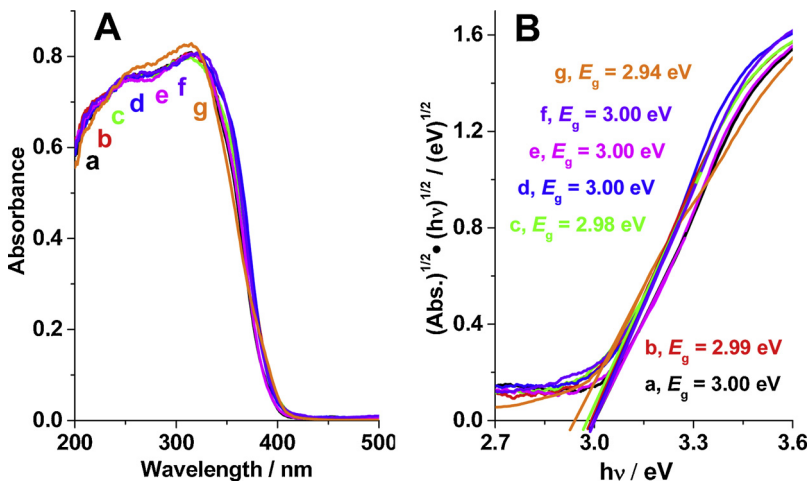


Fig. 6. UV-vis DRS of the samples after extracting silica from the parent nanocomposite for 0 h (SA1) (a), 24 h (SA2) (b), 36 h (SA3) (c), 48 h (SA4) (d), 60 h (SA5) (e) and 72 h (SA6) (f), respectively; Degussa commercial P25 photocatalyst (g). (A) Absorbance versus light wavelength; (B) the square root of Kubelka–Munk functions versus $h\nu$ of the light.

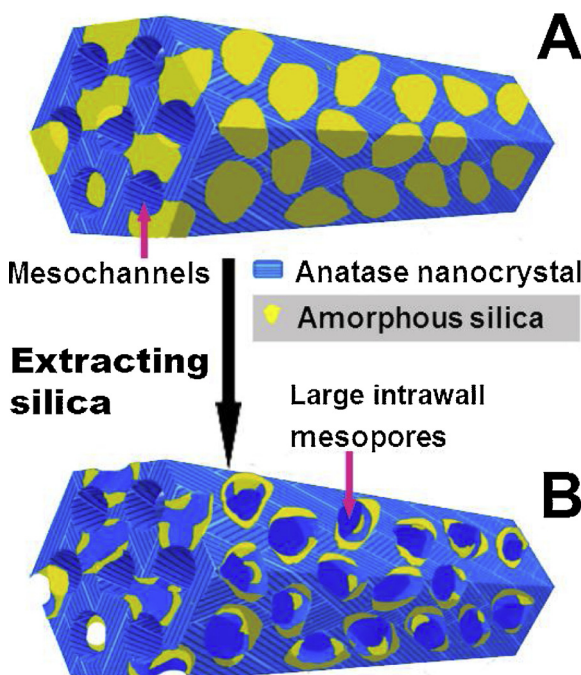


Fig. 7. Scheme for the formation of large intrawall mesopores in the mesoporous anatase crystal-silica nanocomposites. (A), Ordered 2D hexagonal mesoporous anatase crystal-silica nanocomposites; (B), mesoporous anatase crystal-silica nanocomposites with 3D large intrawall mesopores highly connecting the mesochannels.

[Figs. 8A(c–f), S12]. It is inspiring that the diffusivities of MB in the samples with large intrawall mesopores ($\geq 4.8 \text{ nm}$, SA4–SA6) are over 2.5 times higher than that in the samples with small intrawall pores ($\leq 4.2 \text{ nm}$, SA2–SA3), and reach *ca.* 14.7 times faster than that in the 2D parent photocatalyst without intrawall pores (SA1). This should be well ascribed to the contribution of 3D large intrawall mesopores highly linking the channels [Figs. S12–S15]. The enhancement of transport efficiency caused by the larger intrawall pores was also observed in mesoporous silica SBA-15 [48]. However, the AAS (32.6–18.6%) continues to decline obviously [Figs. 8A(c–f), S12, S13]. The alteration tendency of AAS has a negative correlation with the augment of specific surface areas and pore volumes (Table 1), but has a positive correlation with the decrease of surface Si–OH groups in number [Table 2, Fig. S9]. This is because that the adsorption of cationic dyes is predominantly driven by the surface silanol groups [34,35].

Under UV light irradiation, the concentration of MB decreases

exponentially on SA1 with degradation time of photocatalysis [the degradation of MB upon UV light irradiation without catalyst can be neglected [Fig. S16]], and the pseudo-first-order reaction is observed [Fig. 8(A, B)a]. The rate of degradation is measured to be 0.0508 min^{-1} . Excitingly, the specimen SA2 possessing 3D intrawall mesopores of 3.6 nm in size exhibits a considerably high degradation activity to MB (0.213 min^{-1}) [Fig. 8Bb], which is 4.2 and 22.2 times higher than that of the parent SA1 and P25 photocatalyst (0.00958 min^{-1}), respectively. More excitingly, with the enlargement of intrawall mesopores ($4.2\text{--}5.6 \text{ nm}$ in size), the degradation rate continues to rise fast, then drops slowly [Figs. 8B(c–f), S17]. This trend doesn't completely accord with that of surface areas and the number of total acid sites [Table 1–2, Figs. S8, S10], which explicitly indicates that both the surface areas and surface acid sites don't play the predominant role in the variation of activities. Additionally, the bandgap energies also have no contributions to the change of rates [Table 2, Fig. 6]. The reasons for this are that the diffusion efficiency of MB in the 3D interconnected mesochannels, the accessibility and availability of the interior surfaces, etc. can be greatly improved with the increases of intrawall mesopores size and interconnectivity of mesochannels on one hand, which make the activities elevate hugely; on the other hand, the adsorption performance distinctly lowers [Figs. 8A, S13] because of the decrease of surface Si–OH groups in number [Table 2, Fig. S9], which gives rise to the activities drop [34,39]. These two opposite effects make the rates rise rapidly first, arrive to the summit, and then fall gradually. Our previously published results have clearly demonstrated that the synergetic roles of coupled adsorption and photocatalytic oxidation remarkably enhance the activities, but the synchronous role generates the optimal degradation activity [34]. Namely, any adsorption performances deviating from the synchronicity will cause the photocatalytic activities to go away from the best state. Although the adsorption performances go down strikingly, the photocatalysts (SA4–SA6) with large intrawall mesopores ($\geq 4.8 \text{ nm}$) present more excellent activities than that (SA2–SA3) with small mesopores in the walls ($\leq 4.2 \text{ nm}$) [Figs. 8B, S17]. This evidently indicates that the large intrawall mesopores are more advantageous to the elevation of photocatalytic performances. Among the samples with large pores in the walls, SA4 exhibits the optimal activity (0.372 min^{-1}) thanks to the more matched adsorbability [Fig. 8Bd], which is as high as 7.3 times that of SA1, and even up to 38.8 times that upon P25 photocatalyst. The above results fully demonstrate that the large intrawall mesopores highly linking the mesochannels in 3D networks play an overwhelming role in the increments of activities, while the well matched adsorption of SiO_2 to MB around the anatase nanocrystals plays an important synergistic role. Next, we choose SA4 as an example for more detailed evaluations.

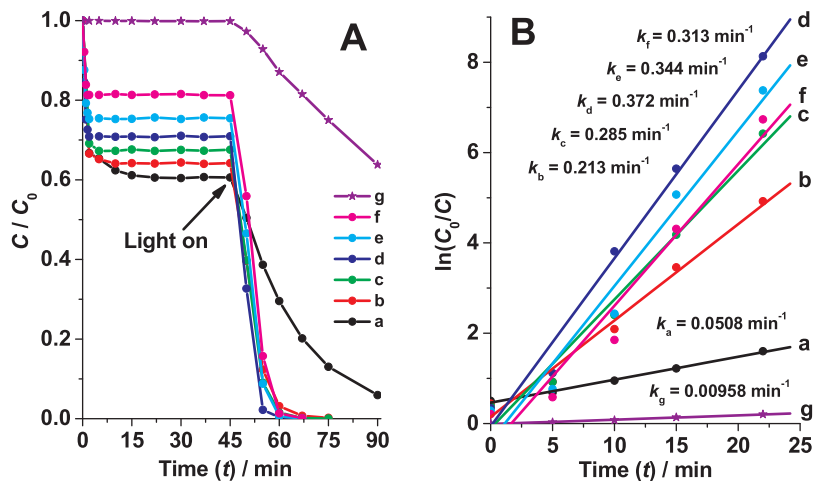


Fig. 8. (A), Adsorption and photocatalytic degradation of MB before and under UV light irradiation in the presence of samples, respectively. (B), Photocatalytic degradation rates of MB on the samples. (a) SA1, (b) SA2, (c) SA3, (d) SA4, (e) SA5, (f) SA6, (g) Degussa commercial P25 photocatalyst.

3.8. Removal percentage of TOC

The removal percentage of TOC for the bulk solution was *ca.* 38.5% after adsorption saturation of MB on the parent photocatalyst [Fig. 9a], which is basically coincident with the result (~39.4%, AAS) measured using UV-vis spectrophotometer [Fig. 8Aa]. On UV light irradiation, the removal percentage continued to increase. When the photocatalytic reaction was carried out for 22 min [Fig. 9a], the removal of TOC rose to *ca.* 61.2% (increased *ca.* 22.7%) [Fig. 9a]. With further reaction to 45 min, approximately 82.5% TOC was removed, testifying that the degradation intermediates were converted into CO_2 and H_2O , etc. For the photocatalyst with large intrawall mesopores connecting the mesochannels in 3D manner, the removal percentage of TOC was *ca.* 30.1% after adsorption saturation [Fig. 9b], which accords with the result (~29.5%, AAS) measured using UV-vis spectrophotometer in essence [Fig. 8Ad], but lower than that of the parent catalyst. Surprisingly, when the reaction was proceeded to 22 min [Fig. 8Ad], the TOC removal was as high as 93.2% (elevated *ca.* 63.1%) [Fig. 9b]. With further irradiation to 30 min, the removal percentage had reached 100%. These are the clear indications that the degradation intermediates are rather easily mineralized into carbon dioxide and water, etc. by our mesoporous photocatalysts with 3D large intrawall mesopores.

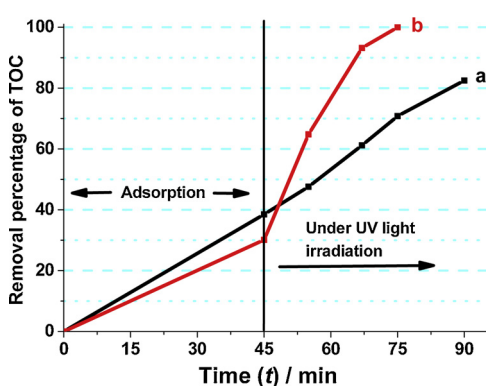


Fig. 9. Removal percentage of TOC of MB aqueous solutions during the course of reactions with the parent sample (a) and the photocatalyst with 3D large intrawall mesopores highly linking the mesochannels (b), respectively; the reaction times corresponding to that in Fig. 8.

3.9. Stability and reusability

The mesoporous nanocomposite possessing 3D large intrawall mesopores performs very fast adsorption to MB before UV light irradiation, it takes only about 2 min to attain adsorption-desorption equilibration in the first run [Fig. 10a]. The AAS (adsorption amount of saturation) is about 29.9%. Under UV light irradiation, the concentration of MB declines exponentially with time and the degradation percentage is as high as 99.7% in 15 min. Similarly, the equilibrium times are still *ca.* 2 min in the next fourteen more cycles [Fig. 10(b-o)], while the AASs are in the range of 27.7–31.4%, which have no significant alterations compared with that in the first run. All the degradation percentages are higher than 99.5%. These results completely illustrate that our composite photocatalysts with large intrawall mesopores in 3D way are quite stable and reusable.

3.10. Transient steady-state concentration of •OH radicals

The steady-state concentration of •OH radicals generated by the parent sample (SA1) without intrawall pores is measured to be $7.510 \times 10^{-13} \text{ M}$ [Figs. 11, S18]. Excitingly, the concentration of •OH produced by the sample SA2 with intrawall mesopores is $32.16 \times 10^{-13} \text{ M}$, which is notably higher (4.3 times) than that of SA1. With the enlargement of intrawall mesopores, the concentrations of •OH go up fast [$51.55 \times 10^{-13} \text{ M}$ (SA4), $63.37 \times 10^{-13} \text{ M}$ (SA6)] [Figs. 11, S18]. These obviously illustrate that the large intrawall mesopores greatly promote the generation of •OH radicals.

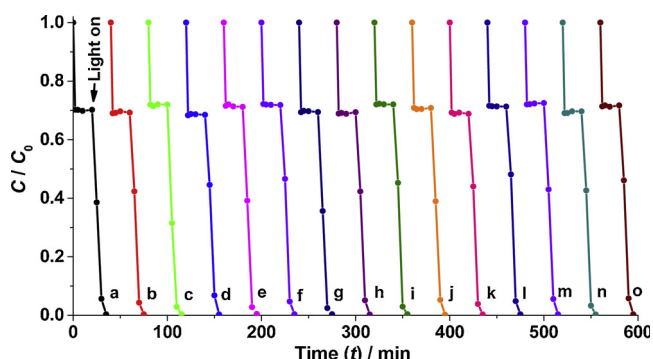


Fig. 10. Investigation of stability and reusability of the mesoporous anatase crystal-silica nanocomposite possessing large intrawall mesopores in 3D networks by repetitively adsorbing and degrading MB. (a)–(o) are the first run to the fifteenth cycle, respectively.

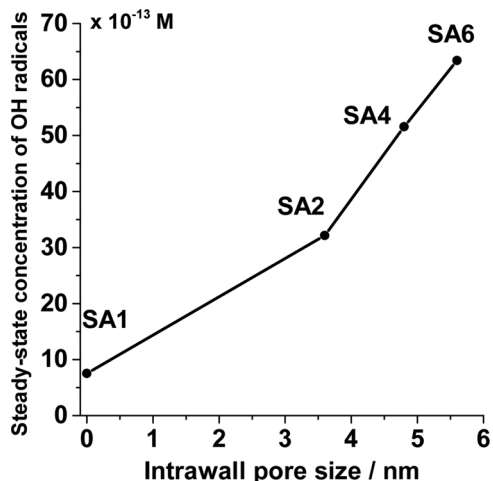


Fig. 11. Transient steady-state concentrations of ·OH radicals generated by the samples of SA1, SA2, SA4 and SA6, respectively.

3.11. Relationship between the activities and the mesostructures with large intrawall mesopores

In our mesoporous anatase crystal-silica nanocomposites, the large intrawall mesopores highly connect the mesochannels in 3D way and countless large pores open on the outer surfaces [Figs. 7B, 12], which are extremely beneficial to the guest molecules to go into and out of, and greatly shorten the diffusion distances and times in the interpenetrated channels, accordingly the diffusion efficiency is tremendously improved. In addition, the opportunity to receive UV light irradiation for the interior surfaces through the large openings and interpenetrated networks of mesopores is hugely enhanced, which lead to a tremendous increment of ·OH radicals in number, and then dramatically raises the photocatalytic activities. Moreover, the SiO_2 nanoparticles enrich the pollutant molecules around the anatase nanocrystals, which can drastically raise the photocatalytic degradation efficiency of TiO_2 , etc. The synergistic promoting of these characteristics makes our mesoporous photocatalysts with 3D large intrawall mesopores generate quite excellent activities. Our results evidently demonstrate that the 3D large intrawall mesopores highly connecting the mesochannels play a very key role in the immense augment of activities, while the well matched adsorbability of silica to MB also has a significant contribution. To the best of our knowledge, such results have not been seen in the literature till now.

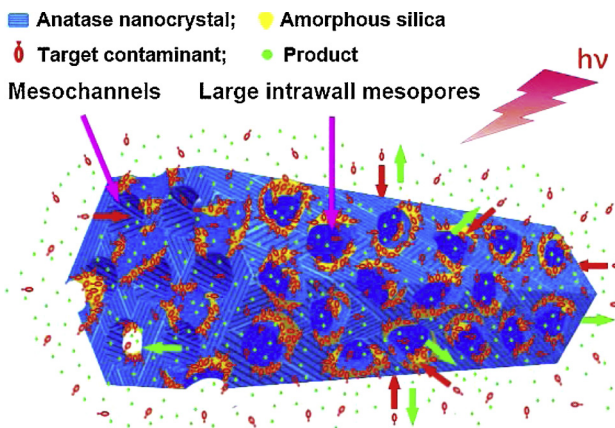


Fig. 12. Scheme for adsorption, diffusion and photocatalytic degradation processes of MB molecules on the mesoporous anatase crystal-silica nanocomposites with 3D large intrawall mesopores.

3.12. Adsorption, diffusion and photocatalytic degradation processes

As we all know, the surface areas of mesoporous photocatalysts stem predominantly from the contributions of their inner surface areas. It is reported that most of the anatase nanocrystals should exist within the mesochannels due to the large internal surface areas, and the generation of ·OH radicals should take place dominantly on the interior surfaces, which deactivates rapidly, and hence hardly diffuse out of the channels owing to the very short diffusion distance (1.3–2.4 nm) inside the cylindrical mesochannels [49]. These are clear indications of the photocatalytic reactions occurring predominantly inside the mesochannels. Moreover, the dual-porous structures can more effectively promote light harvesting, generate more ·OH radicals on the inner surfaces of the photocatalysts, and then markedly elevate photocatalytic efficiency [39,44]. For our mesoporous nanocomposite photocatalysts, the anatase crystals and silica particles similarly coexist predominantly on the internal surfaces [Figs. 7B, 12]. During reactions, the silica particles near the pore openings and on the outer surfaces first adsorb MB molecules. Subsequently, the MB molecules adsorbed diffuse very easily to the silica nanoparticles on the interior surfaces through the numerous openings of large intrawall mesopores and mesochannels, and the 3D interpenetrated mesochannels networks [Fig. 12]. Meanwhile, ·OH radicals generated by the anatase nanocrystals under UV light irradiation react with the nearby MB molecules enriched by the silica particles. Consequently, the molecules are instantaneously degraded into small pieces, and finally mineralized into carbon dioxide, water, etc. Then, CO_2 , etc. could depart very facilely from the reaction places on the interior surfaces to the exoteric surfaces and the solution outside [Fig. 12]. All these processes synergetically, continuously and repeatedly conduct extremely fast thanks to the large intrawall mesopores highly connecting the mesochannels in 3D manner, the high concentrations of ·OH radicals and the suitable adsorption of silica to MB.

4. Conclusions

The mesoporous anatase TiO_2 - SiO_2 nanocomposites with variable intrawall mesopores connecting the mesochannels in 3D networks have been successfully prepared exploiting the approach of first synthesizing anatase crystal-silica nanocomposites possessing ordered 2D hexagonal mesopore channels via “synchronous-assembly” of inorganic precursors with surfactant, then “extracting SiO_2 ”. The results show that the mesochannels in the resulting composites are linked by the uniform 3D intrawall mesopores, and the interconnectivity of channels elevates remarkably with silica removal, but the mesostructured integrities and regularities are retained intact. The size of uniform intrawall pores can be finely tuned in a range of 3.6–5.6 nm by the strategy of adopting a large amount of silica in the walls, a very high crystallization temperature and mild silica extraction. The specific surface areas, pore volumes and the number of surface acid sites increase obviously with the progress of extraction, whereas, the number of surface silanol groups drops fast. Titania is complete anatase crystallization, and the uniform nanocrystals essentially maintained unvaried (ca. 11.2 nm in size) during the whole process of extraction, while the crystallinities of the specimens enhanced gradually. This approach is moderate, simple, controllable and easily repeatable. MB molecules exhibit very high diffusion efficiencies in the mesostructures with large intrawall pores (≥ 4.8 nm), which are over 2.5 times higher than in that with small intrawall pores (≤ 4.2 nm), and arrive to ca. 14.7 times higher than in that without intrawall pores. The photocatalysts with large intrawall mesopores generate much more ·OH radicals than that with small ones. The photocatalytic activities of all the resultant samples are far higher than that of the parent specimen, especially the photocatalysts with large pores in the walls present quite excellent activities. The representative activity (0.372 min^{-1}) is as high as 7.3 times that of the parent material (0.0508 min^{-1}), and even up to 38.8 times that on

Degussa commercial P25 photocatalyst (0.00958 min^{-1}). Our results evidently indicate that the large intrawall mesopores play an overwhelming role in the immense increases of activities, meantime, the well matched adsorption performance of silica to MB plays a vital synergistic role. In addition, all the intermediates degraded were finally converted into CO_2 and H_2O etc. Equally importantly, our photocatalysts are considerably stable and reusable. To the best of our knowledge, such results have not been seen in the literature up to now. Furthermore, this preparation strategy would pave the way for the synthesis of other ordered mesoporous metal-oxides-based materials (such as tantalum pentoxide, niobium pentoxide, etc.) with 3D large intrawall mesopores, proportionate adsorbability and then unexpected photocatalytic performances, etc.

Notes

The authors declare no competing financial interest.

Acknowledgments

This work was financially supported by NSFC (21373056 and 21210004, and 21872036), Science and Technology Commission of Shanghai Municipality (13DZ2275200 and 14JC1400700).

Appendix A. Supplementary data

Molecular structure of MB; TEM images; EDX spectra; variation of specific surface area with extraction time of silica; photocatalytic degradation rates of pCBA by $\cdot\text{OH}$ radicals; etc. Supplementary material related to this article can be found, in the online version, at doi:<https://doi.org/10.1016/j.apcatb.2019.01.055>.

References

- [1] C.J. Vörösmarty, P.B. McIntyre, M.O. Gessner, D. Dudgeon, A. Prusevich, P. Green, S. Glidden, S.E. Bunn, C.A. Sullivan, C.R. Liermann, P.M. Davies, Global threats to human water security and river biodiversity, *Nature* 467 (2010) 555–561.
- [2] S.B. Grant, J.-D. Saphores, D.L. Feldman, A.J. Hamilton, T.D. Fletcher, P.L.M. Cook, M. Stewardson, B.F. Sanders, L.A. Levin, R.F. Ambrose, A. Deletic, R. Brown, S.C. Jiang, D. Rosso, W.J. Cooper, I. Marusic, Taking the “waste” out of “wastewater” for human water security and ecosystem sustainability, *Science* 337 (2012) 681–686.
- [3] M.A. Shannon, P.W. Bohn, M. Elimelech, J.G. Georgiadis, B.J. Mariñas, A.M. Mayes, Science and technology for water purification in the coming decades, *Nature* 452 (2008) 301–310.
- [4] S.Y. Yang, X. Yang, X.T. Shao, R. Niu, L.L. Wang, Activated carbon catalyzed persulfate oxidation of azo dye acid orange 7 at ambient temperature, *J. Hazard. Mater.* 186 (2011) 659–666.
- [5] Y.F. Wang, D. Zhao, W.H. Ma, C.C. Chen, J.C. Zhao, Enhanced sonocatalytic degradation of azo dyes by Au/TiO_2 , *Environ. Sci. Technol.* 42 (2008) 6173–6178.
- [6] Y.Y. Liu, W. Jin, Y.P. Zhao, G.S. Zhang, W. Zhang, Enhanced catalytic degradation of methylene blue by $\text{Fe}_2\text{O}_3/\text{graphene oxide}$ via heterogeneous photo-Fenton reactions, *Appl. Catal. B: Environ.* 206 (2017) 642–652.
- [7] E. Brillas, C.A. Martínez-Huitl, Decontamination of wastewaters containing synthetic organic dyes by electrochemical methods: an updated review, *Appl. Catal. B: Environ.* 166–167 (2015) 603–643.
- [8] S. Chowdhury, R. Balasubramanian, Graphene/semiconductor nanocomposites (GSNs) for heterogeneous photocatalytic decolorization of wastewaters contaminated with synthetic dyes: a review, *Appl. Catal. B: Environ.* 160–161 (2014) 307–324.
- [9] K.S. Hu, X. Xiao, X.F. Cao, R. Hao, X.X. Zuo, X.J. Zhang, J.M. Nan, Adsorptive separation and photocatalytic degradation of methylene blue dye on titanate nanotube powders prepared by hydrothermal process using metal Ti particles as a precursor, *J. Hazard. Mater.* 192 (2011) 514–520.
- [10] H. Métivier-Pignon, C. Faur-Brasquet, P.L. Cloirec, Adsorption of dyes onto activated carbon cloths: approach of adsorption mechanisms and coupling of ACC with ultrafiltration to treat coloured wastewaters, *Sep. Purif. Technol.* 31 (2003) 3–11.
- [11] M. Rafatullah, O. Sulaiman, R. Hashim, A. Ahmad, Adsorption of methylene blue on low-cost adsorbents: a review, *J. Hazard. Mater.* 177 (2010) 70–80.
- [12] C. Leopoulos, D. Doulika, K. Gimouhopoulos, Adsorption of cationic dyes onto bentonite, *Sep. Purif. Rev.* 44 (2015) 74–107.
- [13] M.A.M. Salleh, D.K. Mahmoud, A.W.A.K. Wan, A. Idris, Cationic and anionic dye adsorption by agricultural solid wastes: a comprehensive review, *Desalination* 280 (2011) 1–13.
- [14] M. Zaied, S. Peulon, N. Bellakhal, B. Desmazieres, A. Chausse, Studies of N-demethylation oxidative and degradation of methylene blue by thin layers of birnessite electrodeposited onto SnO_2 , *Appl. Catal. B: Environ.* 101 (2011) 441–450.
- [15] K.M. Lee, C.W. Lai, K.S. Ngai, J.C. Juan, Recent developments of zinc oxide based photocatalyst in water treatment technology: a review, *Water Res.* 88 (2016) 428–448.
- [16] I.A.W. Tan, A.L. Ahmad, B.H. Hameed, Adsorption of basic dye on high-surface area activated carbon prepared from coconut husk: equilibrium, kinetic and thermodynamic studies, *J. Hazard. Mater.* 154 (2008) 337–346.
- [17] H.L. Chiang, K.H. Lin, S.Y. Chen, C.G. Choa, S.D. Pan, Dye adsorption on biosolid adsorbents and commercially activated carbon, *Dyes Pigm.* 75 (2007) 52–59.
- [18] K. Kadivelu, C. Karthika, N. Vennilamani, S. Pattabhi, Activated carbon from industrial solid waste as an adsorbent for the removal of rhodamine-B from aqueous solution: kinetic and equilibrium studies, *Chemosphere* 60 (2005) 1009–1017.
- [19] M. Pelaez, N.T. Nolan, S.C. Pillai, M.K. Seery, P. Falaras, A.G. Kontos, P.S.M. Dunlop, J.W.J. Hamilton, J.A. Byrne, K. O’Shea, M.H. Entezari, D.D. Dionysiou, A review on the visible light active titanium dioxide photocatalysts for environmental applications, *Appl. Catal. B: Environ.* 125 (2012) 331–349.
- [20] Y. Xu, Y. He, X. Cao, D. Zhong, J. Jia, TiO_2/Ti rotating disk photoelectrocatalytic (PEC) reactor: a combination of highly effective thin-film PEC and conventional PEC processes on a single electrode, *Environ. Sci. Technol.* 42 (2008) 2612–2617.
- [21] D.S. Kim, Y.S. Park, Comparison study of dyestuff wastewater treatment by the coupled photocatalytic oxidation and biofilm process, *Chem. Eng. J.* 139 (2008) 256–263.
- [22] S. Yang, H. He, D. Wu, D. Chen, X. Liang, Z. Qin, M. Fan, J. Zhu, P. Yuan, Decolorization of methylene blue by heterogeneous Fenton reaction using $\text{Fe}_{3-x}\text{Ti}_x\text{O}_4$ ($0 \leq x \leq 0.78$) at neutral pH values, *Appl. Catal. B: Environ.* 89 (2009) 527–535.
- [23] K. Yu, S.G. Yang, C. Liu, H.Z. Chen, H. Li, C. Sun, S.A. Boyd, Degradation of organic dyes via bismuth silver oxide initiated direct oxidation coupled with sodium bis-muthate based visible light photocatalysis, *Environ. Sci. Technol.* 46 (2012) 7318–7326.
- [24] K.Y. Lee, A. Mazare, P. Schmuki, One-dimensional titanium dioxide nanomaterials: nanotubes, *Chem. Rev.* 114 (2014) 9385–9454.
- [25] Y.Q. Qu, X.F. Duan, Progress, challenge and perspective of heterogeneous photocatalysts, *Chem. Soc. Rev.* 42 (2013) 2568–2580.
- [26] X.B. Chen, S.S. Mao, Titanium dioxide nanomaterials: synthesis, properties, modifications, and applications, *Chem. Rev.* 107 (2007) 2891–2959.
- [27] J. Schneider, M. Matsuoka, M. Takeuchi, J.L. Zhang, Y. Horiuchi, M. Anpo, D.W. Bahnemann, Understanding TiO_2 photocatalysis: mechanisms and materials, *Chem. Rev.* 114 (2014) 9919–9986.
- [28] P. Innocenzi, L. Malfatti, Mesoporous thin films: properties and applications, *Chem. Soc. Rev.* 42 (2013) 4198–4216.
- [29] X. Li, J.G. Yu, M. Jaroniec, Hierarchical photocatalysts, *Chem. Soc. Rev.* 45 (2016) 2603–2636.
- [30] P.D. Yang, D.Y. Zhao, D.I. Margolese, B.F. Chmelka, G.D. Stucky, Generalized syntheses of large-pore mesoporous metal oxides with semicrystalline frameworks, *Nature* 396 (1998) 152–155.
- [31] B.C. Qiu, M.Y. Xing, J.L. Zhang, Mesoporous TiO_2 nanocrystals grown in situ on graphene aerogels for high photocatalysis and lithium-ion batteries, *J. Am. Chem. Soc.* 136 (2014) 5852–5855.
- [32] W. Zhou, W. Li, J.Q. Wang, Y. Qu, Y. Yang, Y. Xie, K.F. Zhang, L. Wang, H.G. Fu, D.Y. Zhao, Ordered mesoporous black TiO_2 as highly efficient hydrogen evolution photocatalyst, *J. Am. Chem. Soc.* 136 (2014) 9280–9283.
- [33] W.Y. Dong, Y.J. Sun, C.W. Lee, W.M. Hua, X.C. Lu, Y.F. Shi, S.C. Zhang, J.M. Chen, D.Y. Zhao, Controllable and repeatable synthesis of thermally stable anatase nanocrystal-silica composites with highly ordered hexagonal mesostructures, *J. Am. Chem. Soc.* 129 (2007) 13894–13904.
- [34] W.Y. Dong, C.W. Lee, X.C. Lu, Y.J. Sun, W.M. Hua, G.S. Zhuang, S.C. Zhang, J.M. Chen, H.Q. Hou, D.Y. Zhao, Synchronous role of coupled adsorption and photocatalytic oxidation on ordered mesoporous anatase $\text{TiO}_2\text{-SiO}_2$ nanocomposites generating excellent degradation activity of RhB dye, *Appl. Catal. B: Environ.* 95 (2010) 197–207.
- [35] W.Y. Dong, Y.J. Sun, Q.W. Ma, L. Zhu, W.M. Hua, X.C. Lu, G.S. Zhuang, S.C. Zhang, Z.G. Guo, D.Y. Zhao, Excellent photocatalytic degradation activities of ordered mesoporous anatase $\text{TiO}_2\text{-SiO}_2$ nanocomposites to various organic contaminants, *J. Hazard. Mater.* 229 (2012) 307–320.
- [36] S.Y. Choi, B. Lee, D.B. Carew, M. Mamak, F.C. Peiris, S. Speakman, N. Chopra, G.A. Ozin, 3D hexagonal (R-3m) mesostructured nanocrystalline titania thin films: synthesis and characterization, *Adv. Funct. Mater.* 16 (2006) 1731–1738.
- [37] M. Seo, S. Kim, J. Oh, S.-J. Kim, M.A. Hillmyer, Hierarchically porous polymers from hyper-cross-linked block polymer precursors, *J. Am. Chem. Soc.* 137 (2015) 600–603.
- [38] M. Christopher-Orillall, U. Wiesner, Block copolymer based composition and morphology control in nanostructured hybrid materials for energy conversion and storage: solar cells, batteries, and fuel cells, *Chem. Soc. Rev.* 40 (2011) 520–535.
- [39] W.Y. Dong, Y.J. Sun, W.M. Hua, Y.W. Yao, G.S. Zhuang, X.C. Lv, Q.W. Ma, D.Y. Zhao, Preparation of secondary mesopores in mesoporous anatase-silica nanocomposites with unprecedented-high photocatalytic degradation performances, *Adv. Funct. Mater.* 26 (2016) 964–976.
- [40] W.Y. Dong, Y.W. Yao, L. Li, Y.J. Sun, W.M. Hua, G.S. Zhuang, D.Y. Zhao, S.W. Yan, W.H. Song, Three-dimensional interconnected mesoporous anatase TiO_2 exhibiting unique photocatalytic performances, *Appl. Catal. B: Environ.* 217 (2017) 293–302.
- [41] W.Y. Dong, Y.W. Yao, Y.J. Sun, W.M. Hua, G.S. Zhuang, Preparation of three-dimensional interconnected mesoporous anatase $\text{TiO}_2\text{-SiO}_2$ nanocomposites with high photocatalytic activities, *Chin. J. Catal.* 37 (2016) 846–854.
- [42] Y.Z. Li, T. Kunitake, S. Fujikawa, Efficient fabrication and enhanced photocatalytic

activities of 3D-ordered films of titania hollow spheres, *J. Phys. Chem. B* 110 (2006) 13000–13004.

[43] H. Xie, Y.Z. Li, S.F. Jin, J.J. Han, X.J. Zhao, Facile fabrication of 3D-ordered macroporous nanocrystalline iron oxide films with highly efficient visible light induced photocatalytic activity, *J. Phys. Chem. C* 114 (2010) 9706–9712.

[44] X.C. Wang, J.C. Yu, C.M. Ho, Y.D. Hou, X.Z. Fu, Photocatalytic activity of a hierarchically macro/mesoporous titania, *Langmuir* 21 (2005) 2552–2559.

[45] X.N. Hu, L. Huang, J.P. Zhang, H.R. Li, K.W. Zha, L.Y. Shi, D.S. Zhang, Facile and template-free fabrication of mesoporous 3D nanosphere-like $Mn_xCo_{3-x}O_4$ as highly effective catalysts for low temperature SCR of NO_x with NH_3 , *J. Mater. Chem. A* 6 (2018) 2952–2963.

[46] Y.Z. Li, S.J. Kim, Synthesis and characterization of nano titania particles embedded in mesoporous silica with both high photocatalytic activity and adsorption capability, *J. Phys. Chem. B* 109 (2005) 12309–12315.

[47] A.B. Murphy, Band-gap determination from diffuse reflectance measurements of semiconductor films, and application to photoelectrochemical water-splitting, *Sol. Energy Mater. Sol. Cells* 91 (2007) 1326–1337.

[48] V.T. Hoang, Q.L. Huang, M. Eić, T.O. Do, S. Kalaguine, Structure and diffusion characterization of SBA-15 materials, *Langmuir* 21 (2005) 2051–2057.

[49] Y. Shiraishi, N. Saito, T. Hirai, Adsorption-driven photocatalytic activity of mesoporous titanium dioxide, *J. Am. Chem. Soc.* 127 (2005) 12820–12822.